The Journal of Experimental Biology 203, 193–206 (2000)
Printed in Great Britain © The Company of Biologists Limited 2000
JEB2410

HYDRODYNAMICS OF UNSTEADY FISH SWIMMING AND THE EFFECTS OF BODY SIZE: COMPARING THE FLOW FIELDS OF FISH LARVAE AND ADULTS

U. K. MÜLLER*, E. J. STAMHUIS AND J. J. VIDELER

Department of Marine Biology, University of Groningen, The Netherlands

*Author for correspondence and present address: Department of Zoology, University of Cambridge, Downing Street, Cambridge CB2 3EJ, UK (e-mail: ukm20@cam.ac.uk)

Accepted 8 October; published on WWW 22 December 1999

Summary

Zebra danios (*Brachydanio rerio*) swim in a burst-and-coast mode. Most swimming bouts consist of a single tail flick and a coasting phase, during which the fish keeps its body straight. When visualising the flow in a horizontal section through the wake, the effects of the flow regime become apparent in the structure of the wake. In a two-dimensional, medio-frontal view of the flow, larvae and adults shed two vortices at the tail during the burst phase. These vortices resemble a cross section through a large-core vortex ring: two vortex cores packed close together with the central flow directed away from the fish. This flow pattern can be observed in larvae (body length approximately 4 mm) at Reynolds numbers below 100 as well as in adult fish (body length approximately 35 mm) at Reynolds numbers above 1000. Larval vortices differ from those of adult zebra danios mainly in their relatively wider vortex cores (higher ratio of core radius to ring radius) and their lower vortex circulation. Both effects result from the increased importance of viscosity on larval flows. During the coasting phase, larval and adult flows again differ because of the changing importance of viscosity. The high viscosity of the water causes large vortical flows adjacent to the larva's body. These regions of high vorticity represent the huge body of water dragged along by the larva, and they cause the larva to stop almost immediately after thrust generation ceases. No such areas of high vorticity are visible adjacent to adult zebra danios performing a comparable swimming manoeuvre. The rapid decrease in vortex circulation and the severe reduction in the coasting distance due to viscous drag contribute to the high cost that larvae – unlike adult fish – face when using a burst-and-coast swimming style.

Key words: flow, wake structure, particle image velocimetry, burst-and-coast swimming, zebra danio, *Brachydanio rerio.*

Introduction

Many fish propel themselves by running a body wave down their body. This technique is employed by fish larvae and adults alike, in spite of the dramatic changes in the physical environment incurred by an increase in body length of up to three orders of magnitude. Theoretical and experimental research has shown that, with slight modifications, an undulatory swimming style is suitable for the whole range of flow regimes (Gray and Hancock, 1955; Lighthill, 1960, 1969; Webb and Weihs, 1986). In a viscous flow regime, body undulations with a large body wave amplitude exploit resistive forces to generate thrust (Batty, 1981, 1984; Weihs, 1980; Webb and Weihs, 1986). With viscous drag being substantial, continuous swimming is more advantageous because low coasting distances make a burst-and-coast swimming style virtually impossible (Weihs, 1980; Osse and Drost, 1989). In an inertial flow regime, reactive forces are exploited when the swimmer undulates with a body wave amplitude that increases almost exponentially towards the tail. With the drag on an undulating body being several times higher than the drag on a straight body, a burst-and-coast swimming style can save energy compared with continuous swimming (Weihs, 1974).

Fish have responded to the hydrodynamic changes accompanying their development by adapting the ontogeny of their swimming behaviour and morphology in several ways. Fish larvae hatch in the viscous flow regime. To accommodate the constraints imposed by the high viscosity of the water, small fish larvae employ a resistive swimming style. They undulate their body with a large body wave amplitude compared with adult fish (Batty, 1981, 1984). Larvae of several fish species are reported to employ an energetically advantageous continuous swimming style (Weihs, 1980). Some morphological traits in their ontogeny have been interpreted as having hydrodynamic significance, e.g. carp larvae delay the development of the gut, thus keeping their body flexible enough to generate large body waves (Osse, 1990). Adult fish live in the inertial flow regime. Here, undulatory swimmers employ a reactive swimming style with a substantial body wave amplitude only in the posterior part of the body (Wardle et al., 1995). Adults regularly use a burst-

and-coast style, and many have a more streamlined body with a pronounced tail fin.

Other early developmental traits demonstrate an alternative strategy for dealing with the viscous flow regime. Fish larvae allometrically increase their body length L (Fuiman, 1983; Galloway et al., 1999) and their swimming speed (Webb and Weihs, 1986). The growth in length is enhanced until the larva reaches a critical length for the transition to the inertial flow regime (Fuiman, 1983; Osse, 1990; Müller and Videler, 1996). During escape responses, fish larvae can reach swimming speeds of up to $50\,L\,s^{-1}$, carrying them well beyond the viscous flow regime (Fuiman, 1986).

The ontogeny of fish swimming has been studied in only a few species (Fuiman, 1986; Fuiman and Webb, 1988; Batty, 1981, 1984; Hunter, 1972; Vlymen, 1974; Kaufmann, 1990; Darbrowski et al., 1986). In zebra danios (*Brachydanio rerio*), the developmental changes in the swimming performance have been described for escape responses and routine swimming (Fuiman, 1986; Fuiman and Webb, 1988). Because of their small size (L=3–4 mm) and their low swimming speed, up to 98 % of the swimming activities of small zebra danio larvae take place in the viscous or intermediate flow regime (Fuiman and Webb, 1988). Within the first 2 weeks, larval swimming speeds increase almost exponentially, and fish larvae enter the inertial flow regime (Bailey and Batty, 1984).

We used two-dimensional particle image velocimetry (PIV) to obtain a qualitative and quantitative description of the flow patterns generated by larval and adult zebra danios. Analyses and comparisons of the respective flow fields provide insight into the flow regime experienced by a fish larva, as opposed to an adult fish, and provide an estimate of the energetic consequences of changes during development.

Materials and methods

Experimental animals

We chose zebra danios (*Brachydanio rerio* Hamilton), a tropical freshwater species, because both the larval and adult stages use the same burst-and-coast swimming style (Fuiman and Webb, 1988). The fish were cultured in the laboratory at a water temperature of 28 °C. We conducted experiments on sibling larvae of approximately 4 mm body length (7 days post-hatching, yolk sac absorbed, finfold still present) and two adult fish of approximately 35 mm body length.

Flow visualisation

The water movements induced by the swimming fish were visualised using two-dimensional particle image velocimetry (PIV). The experiments on the larvae were conducted in a 60 mm×60 mm×50 mm transparent Perspex container that held five fish larvae at a time. The glass tank for the adults measured 300 mm×150 mm×50 mm and held only one fish at a time. To prevent surface waves distorting the recorded images, the experimental tanks were covered with a Perspex raft. Both tanks were sufficiently large to avoid wall effects in the flow patterns when filming in the centre of the container. Experiments were conducted at 28 °C. The water in the larval container was seeded with nylon spheres (TSI, diameter 4 μm). In the adult tank, we used unexpanded polystyrene spheres (BASF, diameter 20–40 μm) to visualise the flow. The density of both particle types is only slightly higher than the density of fresh water. We assumed that the particles follow the fish-induced flows faithfully and neglected the effects of a very low sinking speed and a slight delay in the response of the particles to the fish-induced water movements. One plane in the centre of the tank was illuminated with a laser light sheet (Coherent Inova 70K krypton laser, light sheet 0.5 mm thick, wavelength λ=647 nm, maximum power P_{max}=1 W). Adult fish seem to adjust their position in the water column to avoid looking directly into the light sheet. In other respects, the swimming behaviour of the fish was unaffected by the laser. We did not train the fish in any way. All observed swimming behaviour was spontaneous. A CCD camera (Adimec MX12, 1024×1024 pixels) was mounted above the water tank normal to the light sheet to record the particle movements induced by the swimming fish. In the case of the fish larvae, the camera was fitted with a 50 mm lens and extension rings (field of view approximately 1 cm×1 cm). The adult fish were filmed using the same filming arrangement, without any extension rings (field of view approximately 7 cm×7 cm). The electronic shutter of the camera was set to 10 ms in the case of the larvae and to 4 ms in the case of the adults to avoid motion blur of the particles. Non-interlaced images (512×512 pixels) of the flow patterns were obtained at a rate of 25 frames s^{-1} and digitised full frame in real time using a purpose-designed digital video-acquisition system (Dutch Vision Systems). Recording was triggered when the fish entered the field of view. The recording system was fitted with a 20-frame pre-trigger recording. Recordings were inspected immediately, and selected sequences were saved uncompressed for later analysis.

Kinematic analysis

Kinematic variables were obtained using an image analysis environment (TIM, Dutch Vision Systems). In each image of a selected sequence, we manually indicated the position of a point on the midline of the fish between the eyes. From the x,y coordinates of this point, we calculated the path of motion using standard linear regression (r for the fitted path was always greater than 0.95). From the frame rate and the linear distance between the head coordinates in consecutive images, we calculated the instantaneous swimming speed. The turning angle was assumed to be the angle between the paths of motion of the coasting fish before and after the turn. The mean acceleration during a burst was calculated from the maximum speed U_m reached during a tail beat and the time between the onset of the tail flick and the instant when the maximum speed was reached. At the end of the active swimming phase, the fish reached the terminal swimming speed U_t. Active distance and active duration were assumed to be the distance covered and the time spent while swimming actively, respectively; resting distance and resting duration were the distance covered whilst coasting and the time spent coasting and resting, respectively.

Bout time and bout distance were the sum of the respective times and distances that the fish was active and resting. We used the same definitions of the bout variables as introduced by Fuiman and Webb (1988). To give a rough indication of the flow regime the fish experiences, we calculated the Reynolds numbers (*Re*) on the basis of the instantaneous swimming speed of the fish and its body length.

Data processing

Particle image velocimetry (PIV)

Flow velocities were calculated by conducting subimage cross-correlation on two successive images (Chen et al., 1993; Stamhuis and Videler, 1995). The cross-correlation takes two subimages from the same area in the flow pattern in two consecutive frames and searches for maximum correlation between the particle patterns. A peak in the spatial correlation coefficient indicates the translational particle displacement in the particular subimage. The correlation analysis of the total flow field yields an array of evenly spaced vectors, each representing the most probable average velocity in the particular subimage. The spatial resolution of the vector fields is determined by the size of the subimage. We used subimages of 33×33 pixels to 39×39 pixels, yielding vector fields of 30×30 vectors to 25×25 vectors.

We aimed at a seeding of 1000–2000 particles in the light sheet. The fish were not affected by this seeding density. With an overlap between subimages of 50 % and subimage sizes between 33×33 and 39×39 pixels, this yielded flow fields of 600–900 velocity vectors.

The size of the subimage is determined by the maximum distance covered by a particle between frames. In the case of very local velocity maxima, there is a trade-off between the precision of the position and the magnitude estimate of the velocity vector. We chose a maximum spatial resolution of the flow field in order to resolve the structure of the vortices at the cost of underestimating the peak flow speeds. Comparison of PIV data with particle tracking results shows an underestimation of the maximum flow velocities of up to 10 %; for medium and low flow velocities, this error is less than 5 %. In the case of one particularly fast larval swimming burst, the maximum flow velocities in the core of the vortex are underestimated by up to 50 % immediately after vortex shedding (t=0–0.2 s). We accepted the loss of these data until 0.2 s after vortex shedding to obtain a more detailed picture of the vortex structure.

Post-processing

The velocity vector field was evaluated using an error routine and interpolated using a two-dimensional spline to fill gaps in the flow field (Stamhuis and Videler, 1995). We derived vorticity and the discriminant for complex eigenvalues from the interpolated velocity vector field. The vorticity ω describes the angular velocity in the flow. The discriminant for complex eigenvalues d describes the amount of divergence and rotation in a gradient field and reaches negative infinity in the centre of vortices (Vollmers et al., 1983); the vector cell with the most negative value of d was assumed to be the centre of a vortex.

Quantitative analysis of the flow

From the velocity vector field, we obtained a quantitative description of the wake shed by the fish. We know from the flow visualisations of McCutchen (1977) that zebra danios shed vortex structures that approximate a vortex ring. Illuminating a two-dimensional cross section through such a

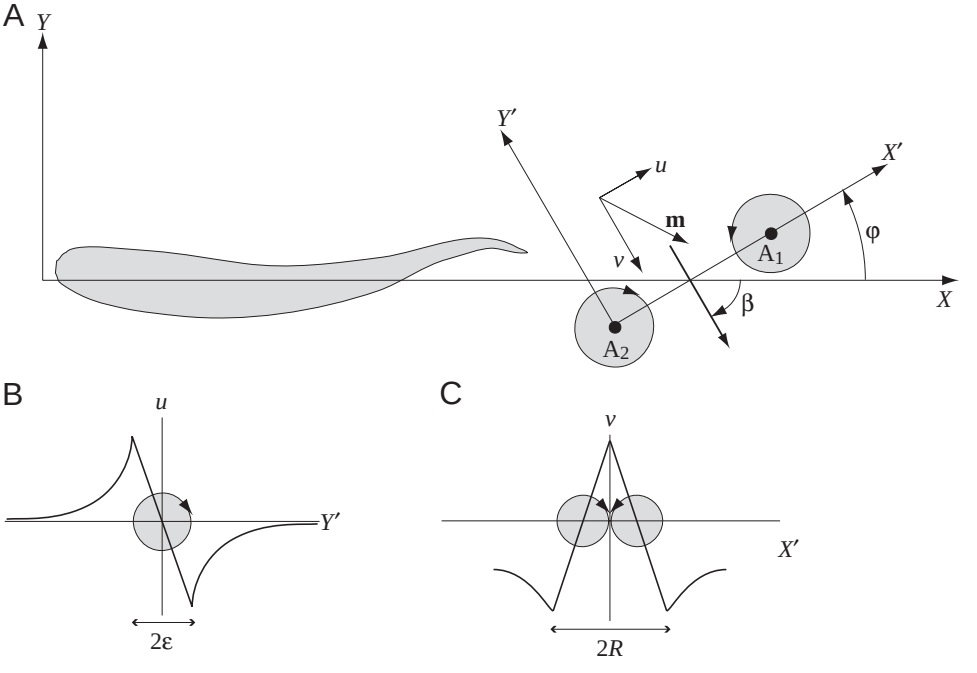

Fig. 1. (A) Coordinate system and notation used to describe the wake. The original image coordinates were transformed so that the fish swam along the X axis. The fish shed the vortices A_1 and A_2. These form a vortex system inclined by a momentum angle φ relative to the path of motion. Between the vortices lies a jet flow (bold arrow) crossing the path of motion at an angle β. The velocity distribution within the vortex system is represented within an X',Y' coordinate system with the X' axis running through the centres of two adjacent vortices. Each velocity vector **m** has velocity components u and v parallel to the X' and the Y' axis, respectively. (B) The u/Y' profile of a vortex. The vortex has a core of diameter 2ε, where ε is the radius of the vortex core. (C) The v/X' profile of two adjacent vortices forming a Hill's vortex sphere. The vortex ring diameter 2R is indicated; R is the radius of the vortex ring.

ring should yield a flow pattern consisting of two vortices separated by a jet flow. The angle β of the jet flow with the new path of motion *X* was assumed to be the average direction of the velocity vectors on the bisector of the line connecting the centre of the vortices A_1 and A_2 (Fig. 1A). The position and velocity of the shed vortices were determined directly from the flow fields using *d* to detect the centre of the vortices. The momentum angle φ of the vortex system with the mean path of motion was also derived from the position of the most negative *d* values in the flow field (Fig. 1A).

From the tangential flow velocities *v* around a vortex centre *A* (Fig. 1), we obtained the circulation Γ of the vortex, with *C* being a closed curve around the vortex centre (section 2.6 in Batchelor, 1967):

$$\Gamma = \int_C v \mathrm{d}Y' . \quad (1)$$

We assume that all the momentum is contained in the vortex structure shed in the wake. The impulse *p* can be derived from the radius *R* of the vortex ring and the circulation Γ according to (paragraph 162 in Lamb, 1932):

$$p = \rho_{water} \Gamma \pi R^2 , \quad (2)$$

where ρ_{water} is the density of water. This approach assumes that zebra danios shed single, small-core circular vortex rings of radius *R*. At the other extreme of possible ring shapes is Hill's vortex sphere. For such a large-core vortex ring, the ring impulse is calculated from the mean ring radius *a* according to (Kumar et al., 1995):

$$p = \rho_{water} \Gamma \pi a^2 , \quad (3)$$

with *a* being a function of the ring radius *R* and the core radius ε.

To characterise the shed vortices, we determined the following variables (Fig. 1B,C): the velocity component *u* parallel to the *X*′ axis of the vortex system; the velocity component *v* parallel to the *Y*′ axis; the momentum angle φ of the vortex system with the mean path of motion *X*; the radius ε of the vortex core; the radius *R* of the vortex ring; the mean radius *a* of the vortex ring. From the velocity components *u* and *v*, we derived the profiles of *u* and *v* along the *Y*′ and *X*′ axes, respectively (Fig. 1B,C). The radius ε of the vortex core was assumed to be half the distance between the velocity extremes in the *u*/*Y*′ profile. The vortex ring radius *R* was defined as half the distance between the centres of the two vortex cores in the *v*/*X*′ profiles. The mean radius *a* of the vortex ring was calculated from the area occupied by elevated vorticity (section 7.2 in Batchelor, 1967). We also derived the non-dimensionalised mean core radius α from the core radius ε and the mean ring radius *a*. For a Hill's vortex sphere, α is $\sqrt{2}$, otherwise $0<\alpha<\sqrt{2}$ and for small-core vortices $\alpha<0.25$ (Norbury, 1973).

Results

The routine swimming of zebra danios, both larvae and adults, is of a burst-and-coast style. Brief acceleration periods of one or two tail strokes are followed by a deceleration period when the fish coasts. Coasting larvae keep their body straight. In larvae, we only observed single tail flicks. Decelerating adults either coast with a straight body or continue moving their body with a reduced body wave amplitude, thus approaching a more continuous swimming style. Swimming bursts followed by coasting are often associated with a change in swimming direction for both larvae and adults.

Of 95 recorded sequences, 30 were selected in which the fish swam horizontally in the camera's field of view in the light sheet. We analysed 17 larval and 13 adult swimming episodes. Our observations of swimming speeds, active and resting distances as well as active and resting durations for both larvae and adults agree with the kinematic study of Fuiman and Webb (1988) (Table 1). Thus, the PIV arrangement with its bright light sheet illuminating just one plane in the otherwise dark tank does not influence the swimming behaviour in any measurable way.

Two sequences of larval swimming bouts and one of an adult were selected for analysis of the wake morphology and momentum. These sequences were chosen for their high density of original velocity vectors. Hence, the flow fields contain less than 1 % interpolated vectors.

Burst phase

In the 17 larval and 13 adult swimming episodes analysed, the burst phase consists of one or, more rarely, two tail-beat cycles. Both larvae and adults reach a maximum speed of approximately $4\,L\,s^{-1}$ after approximately 10 % of the total bout time (Table 1). Larvae cover approximately half the bout

Table 1. *Morphological and kinematic variables*

	Symbol	Larvae	*N*	Adults	*N*
Body length (mm)	*L*	4.1±0.1	10	34.8±0.4	2
Maximum velocity (mm s^{-1})	U_m	15.7±4.5	27	129.9±15.5	4
Mean acceleration (mm s^{-2})		206±93	27	1623±194	4
Active distance (mm)		0.94±0.34	26	7.90±1.87	4
Resting distance (mm)		1.11±0.43	26	30.06±9.61	2
Active duration (s)		0.08±0.03	27	0.14±0.04	2
Resting duration (s)		0.92±0.03	21	0.86±0.04	2

Values are means ± S.D.

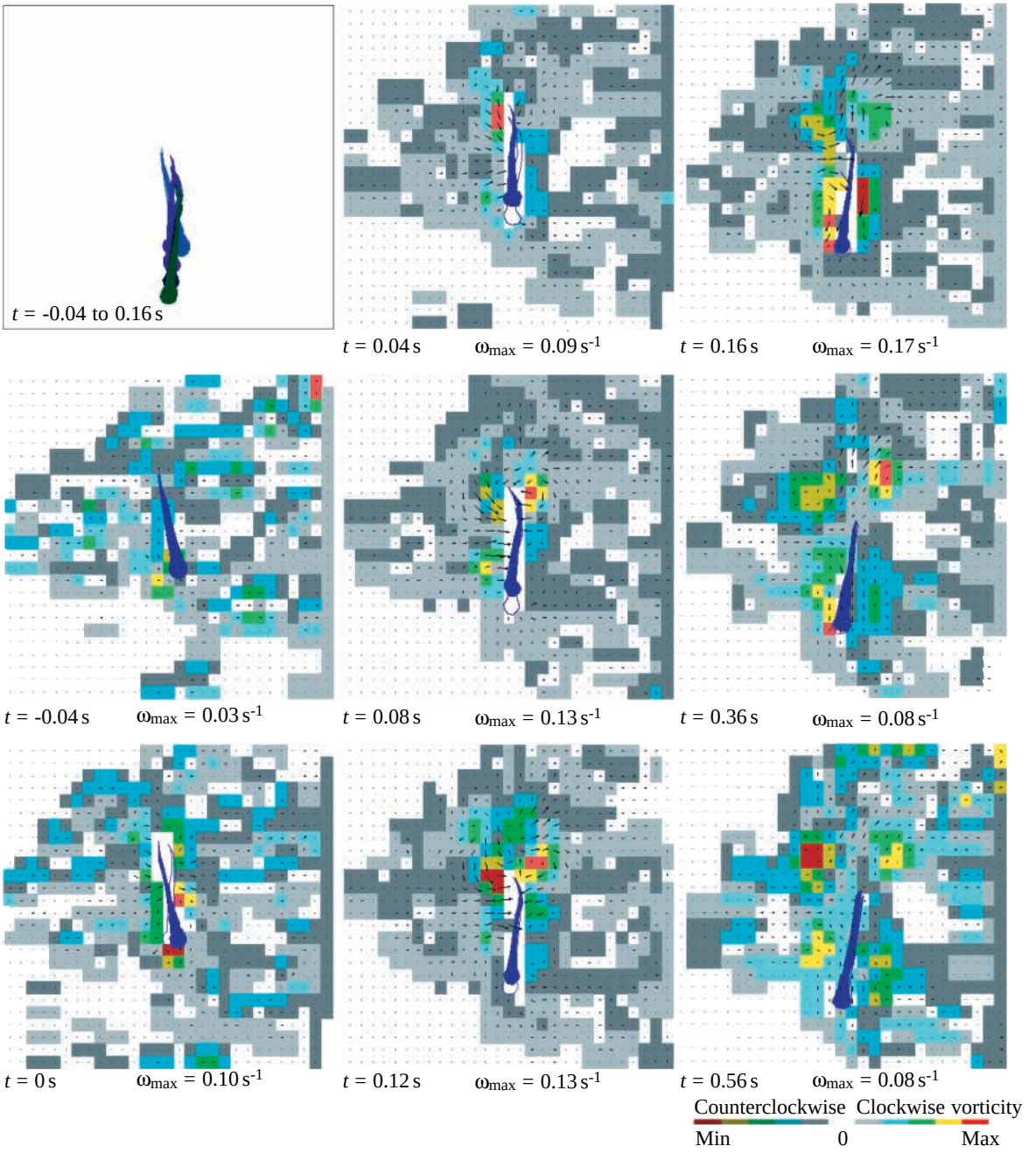

Fig. 2. Larval swimming burst. Silhouettes of the fish from before the initiation of the swimming bout (at time t=–0.04 s) until time t=0.56 s after the initiation. The vorticity (coloured squares) and flow velocity vector field (black arrows) around a larva during a swimming bout are shown. The velocity vectors are magnified by a factor of 5 relative to the length of the fish and the size of the field of view. The field of view is 13.5 mm×13.5 mm. See text for further explanation. ω_{max}, maximum vorticity. The open outline shows the fish 0.04 s after the filled outline.

distance actively, whereas adults cover the larger part of the bout distance coasting. Larvae come to a total standstill before initiating the next tail flick. Adults usually initiate the next tail flick before total standstill. During the burst, larval Reynolds numbers were between 10 and 100, adult Reynolds numbers were approximately 5000.

In the first swimming bout chosen for detailed hydrodynamic analysis, the larva changes its swimming direction by 16 ° and reaches a maximum swimming speed of 17.5 mm s^{-1} (4.3 L s^{-1}). In the burst phase, the larva moves its tail to the right and left, generating two vortices in the wake. Fig. 2 gives a two-dimensional impression of the flow generated in the medio-frontal plane of the larva. The fish performs a small tail flick to the right of the animal (Fig. 2, t=–0.04 s) followed by a tail flick to the left as part of a larger deformation of the body (Fig. 2, t=0 s). The first tail movement

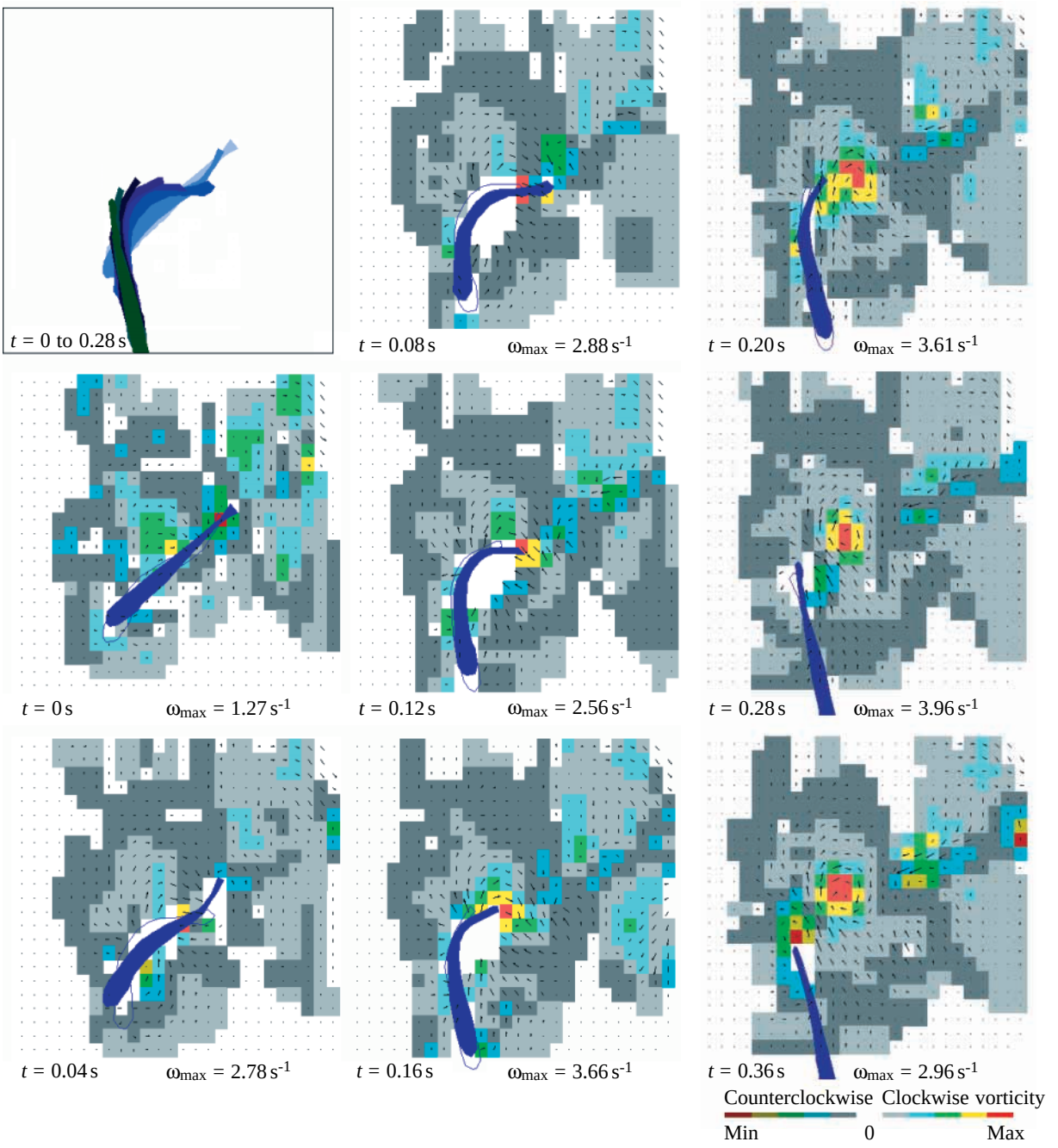

Fig. 3. Adult swimming bout. Silhouettes of the fish from the initiation of the swimming bout (t=0 s) until t=0.36 s after the initiation. The vorticity (coloured squares) and flow velocity vector field (black arrows) around an adult during a swimming bout are shown. The velocity vectors are magnified by a factor of 5 relative to the length of the fish and the size of the field of view. The field of view is 71 mm×71 mm. See text for further explanation. ω_{max}, maximum vorticity. The open outline shows the fish 0.04 s after the filled outline.

to the right of the larva generates very little flow and no noticeable displacement of the larva. The tail movement to the left reorients the larva into its new swimming direction. The substantial bending of the body also creates suction and pressure flows adjacent to the larva. The larva is propelled forward, reaching its maximum forward swimming speed immediately after changing its orientation (Fig. 2, t=0.04 s). It coasts forward while straightening its body (Fig. 2, t=0.04–0.20 s), its coasting speed decreasing steadily. The suction flow created by the bending on the right side of the larva travels down the body, along with the maximum lateral excursion of the body. It reaches the tail as the fish finishes straightening its body, and the vortical flow is shed into the wake, forming a counterclockwise vortex to the right of the fish. As the tail stops its lateral movement, a clockwise vortex is shed from the tail to the left of the fish. The two vortices are

Table 2. *Wake and vortex variables at time* t *after the initiation of the tail flick*

		Larva		
	Symbol	Slow burst t=0.16 s (0 s)	Fast burst t=0.16 s (0.16 s)	Adult t=0.20 s (0 s)
Turning angle (degrees)		16	110	57
Jet angle (degrees)	β	18	11	49
Jet velocity (mm s^{-1})		3.4	3.7	9.6
Momentum angle (degrees)	φ	90	97	48
Vortex velocity (mm s^{-1})		0.05	0.1	1.4
Vortex core radius (mm)	ε	1.1	1.2	4.7
Vortex ring radius (mm)	R	0.9	0.7	7.9
Mean ring radius (mm)	a	1.8	1.3	12.1
Circulation (mm^2 s^{-1})	Γ	12	16	290
Angular velocity of the core (s^{-1})		0.45	0.39	0.20
Vortex impulse (N s)	$p(a)$	9.6×10^{-8}	14.5×10^{-8}	9.8×10^{-5}
	$p(R)$	3.2×10^{-8}	2.3×10^{-8}	5.8×10^{-5}

Time after the vortex was shed is given in parentheses.

noticeable as an increase in the vorticity behind the animal (Fig. 2, t=0.16 s). The vortices move away from the larva and away from the mean path of motion at a speed of approximately 0.2 mm s^{-1} in an earth-bound frame of reference. The jet between the two vortices points away from the larva and is oriented almost perpendicular to the axis X' of the vortex system. The momentum angle of the vortex system with the new path of motion is 90 °, the angle of the jet with the new path of motion is 18±5 ° (mean ± S.D., N=5 velocity vectors in the central jet region of Fig. 2, t=0.16 s) (Table 2). The mean flow speed in the jet is 3.4±0.3 mm s^{-1} (mean ± S.D., N=5 velocity vectors in the central jet region of Fig. 2, t=0.16 s), which is equivalent to 19 % of the larva's maximum swimming speed (Table 2). Vorticity is elevated not only in the wake, but also adjacent to the larva's body. A counterclockwise flow component can be detected to the left and a clockwise flow component is visible to the right of the larva. After a larval tail flick, the following flow pattern emerges in the medio-frontal plane of the animal: in the wake, the two vortices are probably a cross section through a vortex ring shed at the tail; on the body, vortical flow components become visible forming a typical viscous flow pattern around a bluff body at low Reynolds numbers (van Dyke, 1982).

The adult tail flick sequence selected for hydrodynamic analysis shows a swimming burst in which the fish reaches a maximum speed of 130 mm s^{-1} (3.7 L s^{-1}) and turns 57 ° to the left (Fig. 3). Fig. 3 shows the flow in the medio-frontal plane of the fish. The adult fish initiates the swimming bout by assuming an S-shape (Fig. 3, t=0 s). This generates a weak suction flow at the peduncle where the flow follows the lateral movement of the posterior body. This most posterior suction flow intensifies as this initial body wave increases in amplitude towards the tail (Fig. 3, t=0.04 s) and is shed into the wake as a weak counterclockwise vortical flow when the tail changes direction (Fig. 3, t=0.08 s). Furthermore, the fish generates a large suction and pressure flow half-way along the body where it bends sharply as the head starts pointing into the new swimming direction (Fig. 3, t=0.04–0.12 s). This strong suction/pressure flow travels down the body along with the area of high curvature. It reaches the tail as the body begins to straighten and is shed into the wake as a clockwise vortex (Fig. 3, t=0.20 s). The tail continues to move to the right of the fish until the body is straightened. When the movement of the tail stops and the fish has assumed a coasting position, a second counterclockwise vortex is shed from the tail. This vortex forms a pair together with the clockwise vortex shed 0.16 s earlier. As the second vortex is shed, the fish reaches its maximum velocity in the new swimming direction. Like the larva, the adult flow field shows a vortex pair in the wake. After being shed, the adult vortices move backwards and sideways at a speed of 1–2 mm s^{-1}. The vortex shed first to the left-hand side of the fish moves slightly faster than the second vortex. The jet between the vortices is perpendicular to the vortex system and points away from the fish at an angle of 49±10 ° (mean ± S.D., N=37) with the new path of motion (Table 2) (Fig. 3, t=0.28 s). The average speed of the jet is 9.6±2.6 mm s^{-1} (N=4) or 7 % of the fish's maximum swimming speed (Table 2). In the medio-frontal cross section of the fish, the adult tail flick produces the following flow pattern: a single vortex pair in the wake which, like the vortex system in the larval wake, probably constitutes a cross section through a vortex ring. As expected for a streamlined body in an inertial flow regime, no large area of elevated vorticity can be observed adjacent to the adult's body.

Coasting phase

In all burst-and-coast sequences analysed, larvae cover a total distance of approximately half a body length during one burst-and-coast bout (Table 1). Half the distance is covered actively, the other half by coasting. Adult fish cover a total distance of approximately one body length during one swimming bout. Of this distance, 20 % is covered actively, the remainder is covered by coasting. The coasting speed of a larva halves within 15 % of the total bout time. Adults take twice as long (approximately 30 % of the total bout time) to decelerate to half their terminal swimming speed.

In the sequence selected for hydrodynamic analysis, a larva of 4.1 mm body length reaches a maximum swimming speed of 17.5 mm s^{-1} 0.16 s after the start of the burst and 0.08 s before the body was totally straightened. During this time, the larva covers 1.3 mm. It comes to a virtual halt 0.4 s after reaching its maximum speed, covering a total distance of 1.2 mm coasting. By the time the larva has assumed a straight body, its speed has already dropped to the terminal speed of 39.6 mm s^{-1} and the distance covered by coasting with a straight body is 0.4 mm. The coasting produces a typical viscous flow field with two large vortices, one to the left and the other to the right of the larva (Fig. 4A). Using elevated vorticity as an indicator of the area over which the fish influences the flow, the distribution of vorticity in the fluid

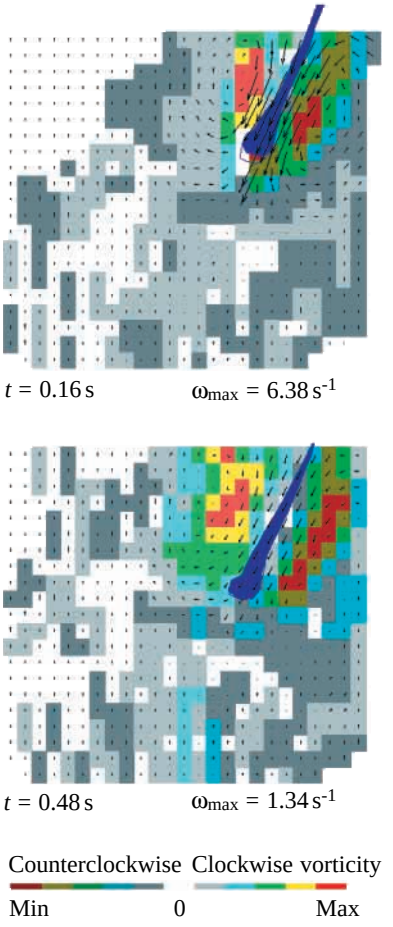

Fig. 4. Coasting larva. The vorticity (coloured squares) and flow velocity vector field (black arrows) around a coasting larva (body length 4.1 mm) 0.16 s and 0.48 s after the initiation of a tail flick. The terminal velocity v_0 of the larva reached during the tail flick was 39.6 mm s^{-1}. The instantaneous swimming speeds of the fish are 5.7 mm s^{-1} at t=0.16 s and 0.5 mm s^{-1} at t=0.48 s. The velocity vectors are magnified by a factor of 5 relative to the length of the fish and the size of the field of view. The field of view is 13.5 mm×13.5 mm. See text for further explanation. ω_{max}, maximum vorticity. The open outline shows the fish 0.04 s after the filled outline.

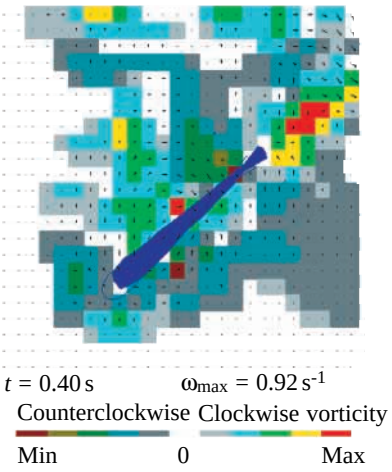

Fig. 5. Coasting adult. Vorticity (coloured squares) and flow velocity field (black arrows) around a coasting adult (body length 35 mm) are shown. The instantaneous swimming speed of the fish is 81 mm s^{-1}. The figure represents the flow 0.4 s after the initiation of the tail flick, and the terminal speed reached during the tail flick is 176 mm s^{-1}. The velocity vectors are magnified by a factor of 5 relative to the length of the fish and the size of the field of view. The field of view is 71 mm×71 mm. See text for further explanation. ω_{max}, maximum vorticity. The open outline shows the fish 0.04 s after the filled outline.

shows that the larva drags along a huge body of water (Fig. 4B).

An adult fish of 35 mm body length coasting at a terminal swimming speed of 176 mm s^{-1} halves its speed within the first 0.2 s, covering a distance of 29 mm. The fish initiates the next burst before it comes to a total standstill. The only visible flow adjacent to the fish's body is the source effect of the head pushing the water away (Fig. 5). In the wake, a weak flow towards the fish develops from the moment when the fish starts coasting (also visible in Fig. 3, from top right to the centre of the flow fields). Vorticity is much lower in the adult flow field. It is highest in the wake rather than to the left and right of the fish.

Vortex morphology and the energetics of the wake

Given that vortices cannot end free in the fluid, it is justifiable to assume that the two vortices seen in the two-dimensional flow fields represent a cross section through a vortex ring. To characterise this ring and ultimately to estimate the impulse of the wake, we need to determine the shape and size of the shed vortices and to measure the flow velocities.

To obtain a detailed velocity profile from the larval wake, additional recordings were made at a higher magnification, sacrificing a total overview of the flow pattern for a more detailed picture of the vortices in the wake. Fig. 6 shows a larva performing a burst lasting 0.04 s leaving the field of view at the lower left-hand corner at an estimated swimming speed of 100 mm s^{-1} (Fig. 6A). Since the swimming manoeuvre was completed within one recording frame, we have no information on the swimming kinematics other than a rough indication of the swimming direction. The wake shed by the fish larva consists of the same basic vortex pattern as the flow field of a slower larval burst (Fig. 2, t=0.16 s). The viscous vortex structure, visible adjacent to the larva's body in the slow burst sequence (Fig. 2, t=0.16 s), is only partially included in the lower left-hand corner of the flow field (Fig. 6B,C). The vortex structure shed in the wake, however, is clearly visible: in the medio-frontal plane of the larva, a vortex pair is generated by the tail flick. This vortex pair is interpreted as a cross section through a vortex ring that forms in the wake of the larva. The jet through the centre of the vortex ring has a mean speed of 3.7±1.2 mm s^{-1} (N=4 velocity vectors at equal distance from both vortex cores in the central jet region of Fig. 6B). The jet angle with the estimated new path of motion is 11±4° (N=14 velocity vectors in the central jet region of Fig. 6B). The momentum angle of the tail flick vortex ring with the estimated path of motion is 97°.

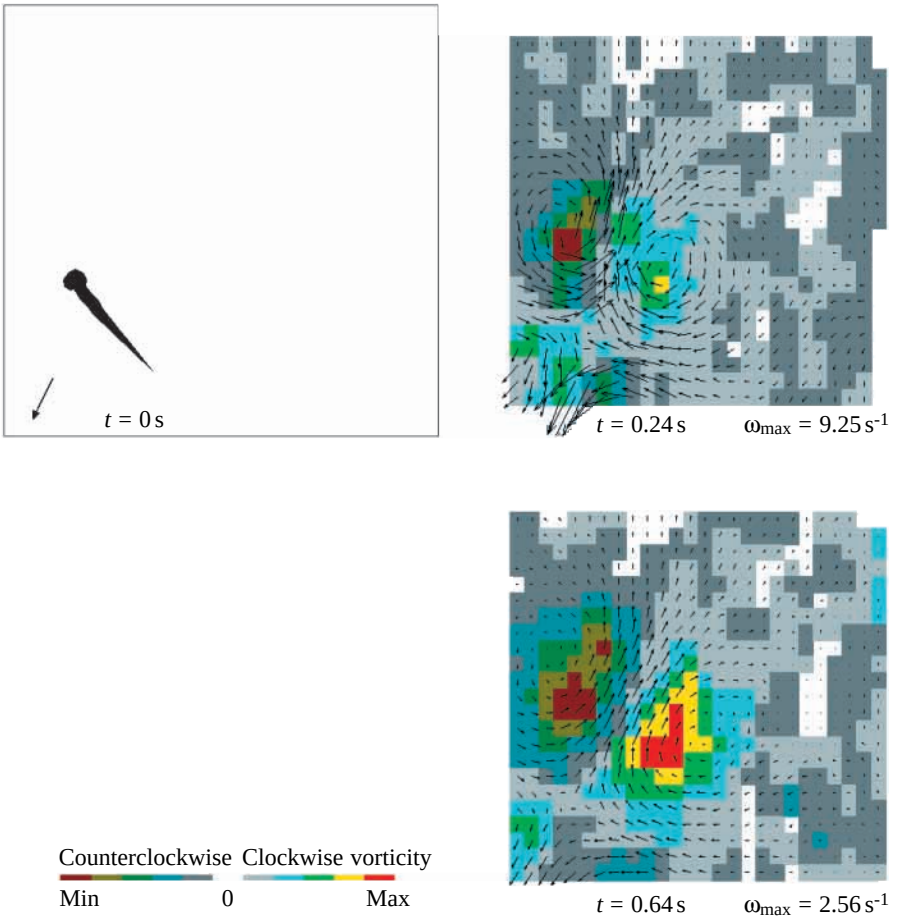

Fig. 6. Swimming burst of a larval fish. The position of the larva before the escape response is shown in the left-hand panel. The larva left the field of view through the lower left corner (swimming direction indicated by the arrow). The vorticity (coloured squares) and velocity flow field (black arrows) generated by the larva, 0.24 s and 0.64 s after the initiation of the burst are shown in the right-hand panels. The two vortices moved away from the larva in an earth-bound frame of reference. The velocity vectors are magnified by a factor of 5 relative to the length of the fish and the size of the field of view. The field of view is 10 mm×10 mm. ω_{max}, maximum vorticity.

Larval and adult wakes differ little in their velocity profiles. The u/Y' profiles of the larval and adult vortices show a vortex core in solid body rotation surrounded by a potential flow (Fig. 7A–C). The vortex ring profiles v/X' show the two vortices of the ring cross section shed close together. Their vortex core flows comprise a jet region (Fig. 7D–F).

The larval ring radius R, measured as half the distance between the vortex cores, is smaller than the core radius ε at the moment of vortex shedding (Fig. 2; Table 2). At the same time, the ratio of mean ring radius a to ring radius R is 2, as predicted for a Hill's vortex sphere, with a vorticity distribution approaching the spherical profile of a Hill's vortex sphere (Fig. 2, t=0.12 s; Fig. 6, t=0.24 s). In all the flow fields analysed, the non-dimensionalised mean core radius α is close to $\sqrt{2}$ (with $\sqrt{2} \geqslant \alpha > 0$ and $\alpha = \sqrt{2}$ for a Hill's spherical vortex) (Norbury, 1973). All this is evidence suggesting that fish larvae shed large-core vortex rings similar to a spherical Hill's vortex sphere. The viscous length scale of the vortex $\sqrt{4\nu T}$ (Acheson, 1990) (where ν is the kinematic viscosity of water and T is tail-beat period) is only a little smaller than the core radius and larger than the ring radius. This suggests that viscous diffusion plays a large role in larval vortices. As the vortex ring diffuses over a time course of 0.4 s, the ring radius R more than doubles while the angular velocity of the core drops rapidly by an order of magnitude (Fig. 8). The widening of the vortex core is too small to be detectable at this spatial resolution. In the wake of the fast larval burst, recorded at a higher magnification (Fig. 6), the vortex core radius ε increases visibly. In spite of the differences in swimming speed, the values for ε, R and α are similar for both larval recordings (Figs 2, 6).

An adult tail flick generates vortex cores and vortex rings several times wider than the vortex structures shed by larval fish in accordance with a larger tail-beat amplitude (Figs 7, 8). Adult vortex rings have large cores with a mean non-dimensional core radius α of just under 1.0. The vorticity distribution deviates further from the spherical pattern of a Hill's vortex sphere than the larval vortices (Fig. 3, t=0.36 s). All this evidence suggests that the adult also sheds large-core vortices. But, unlike larval vortices, these do not resemble a Hill's sphere very closely. The viscous length scale is a quarter of the core radius. Hence, viscous diffusion is less important for the time course of the adult vortex. The angular flow velocity of the adult cores is initially similar to the larval values, but drops little over the course of one swimming bout. Over the time course of one coasting period (0.6 s), the ring radius decreases by almost half while the core radius stays more or less constant.

We conclude that both larvae and adult fish shed large-core vortex rings and we expect impulse estimates assuming a large vortex core to be more accurate than the small-core estimates.

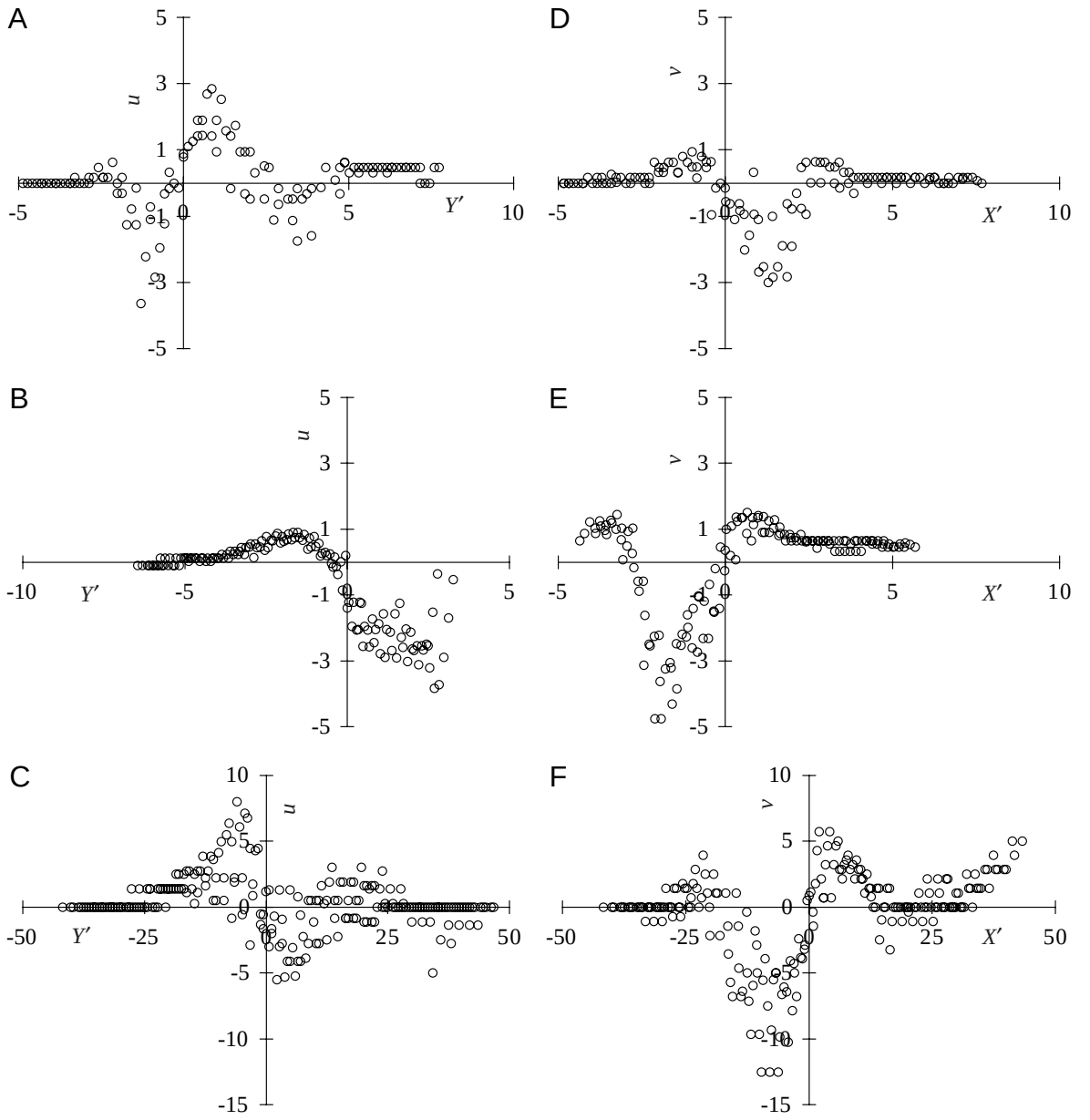

Fig. 7. Velocity profiles of the vortices shed by the larval and the adult fish. The vortex profiles of Fig. 7A and D, B and E, C and F, are derived from the swimming sequences depicted in Figs 2, 6 and 3, respectively, though they may be based on a flow field not depicted in those figures. (A) Slow larval burst: u/Y' profile of the vortex to the right-hand side of the larva in Fig. 2 at t=0.20s, t=0.04 s after shedding. (B) Fast larval burst: u/Y' profile of the vortex to the left-hand side of the larva in Fig. 6B, 0.24 s after shedding. (C) Adult tail flick: u/Y' profile of the vortex to the left-hand side of the animal in Fig. 3 at t=0.32 s, 0.04 s after shedding. (D–F) v/X' profiles of the same vortices used for the u/Y' profiles. See Fig. 1 for definitions of axes.

Hence, to calculate the impulse, we use the mean ring radius a, derived from the vorticity distribution, and the circulation Γ, derived by integration from the velocity profiles. We obtained estimates for the circulation of the vortex structures in the wake of a fast larval burst (Fig. 6), a slow larval burst (Fig. 2) and an adult burst (Fig. 3) from the moment the vortex was shed to up to 1 s later. The data on the fast larval vortex are of sufficient quality to show viscous diffusion of the circulation over the course of 1 s (Fig. 8). The spatial resolution of the slow larval vortex is too low to yield reliable circulation estimates, but its order of magnitude corresponds to the values for the fast larval burst. The adult vortex ring contains circulation that is an order of magnitude greater than the larval circulation. The time courses of the adult circulation and ring radius are more irregular than in the larval vortex rings. This might indicate that adult rings, although still laminar, show some oscillation in shape.

We obtained impulse values for the moment the vortex ring was shed (Table 2). Assuming a small core (equation 2) severely underestimates the impulse compared with the large-

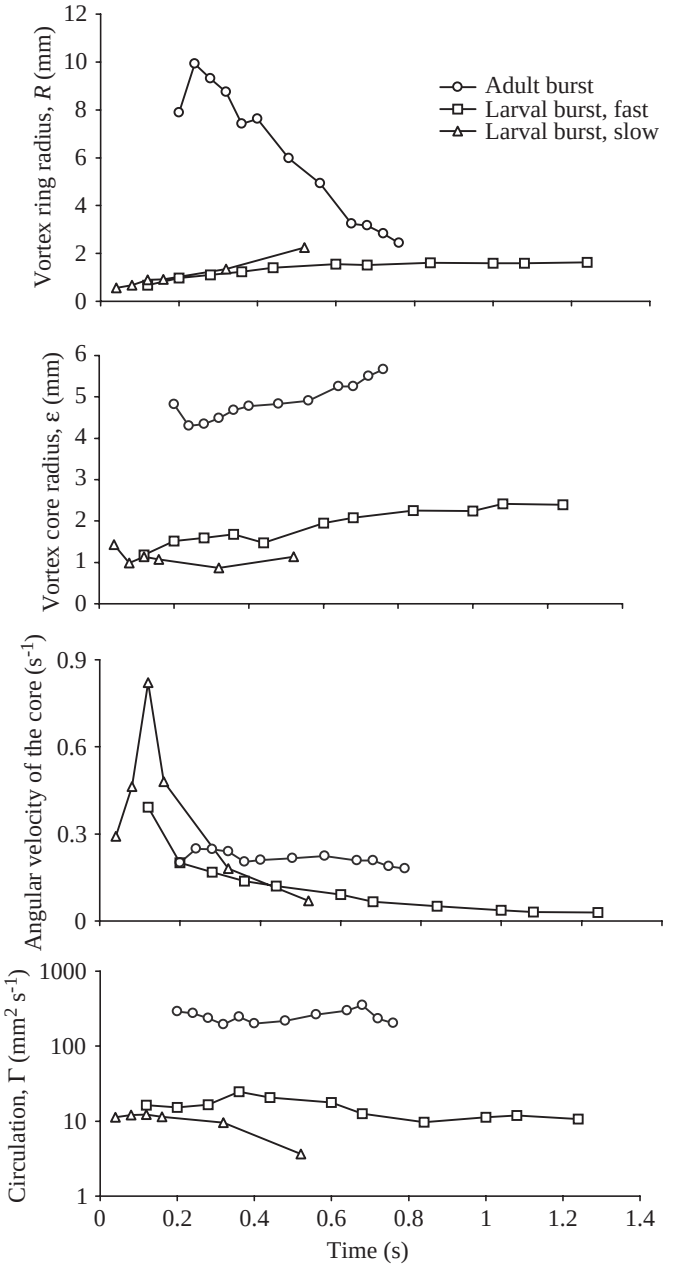

Fig. 8. Time course since the initiation of a tail beat (t=0 s) of the vortex ring radius R, the vortex core radius ε, the angular velocity of the vortex core and the circulation Γ of the first vortex shed during a slow larval burst (flow fields in Fig. 2), a fast larval burst (flow fields in Fig. 6) and an adult burst (flow fields in Fig. 3).

core impulse (equation 3). For larval vortex rings, the small-core prediction is several times lower than the large-core value of 9.6×10^{-8} N s (flow fields of Fig. 2) and 14.5×10^{-8} N s (flow fields of Fig. 6). The values for the adult vortex rings are 5.8×10^{-5} and 9.8×10^{-5} N s for small- and large-core rings, respectively. Because of the larger size of adult vortices, the adult impulse is three orders of magnitude greater than the larval impulse at the moment of vortex shedding. With the impulse in the wake being a measure of the impulse gained by the fish, this means that the thrust provided by larval vortices compared with adult vortices scales according to the body mass of the larva and adult.

Discussion

Comparing hydrodynamic and kinematic impulse estimates

Estimating propulsive impulse from the wake behind an animal has proved to be problematic. Spedding et al. (1984) and Spedding (1986, 1987) could not match the energy estimates derived from the wake with the energy requirements to support a bird in the air. McCutchen (1977), however, found a higher impulse in the wake than his estimates from the swimming speed of the fish.

The backward momentum shed by the fish in the wake must equal the forward momentum gained by the fish. The latter can be estimated from the time course of the fish's coasting speed and its body mass. This approach yields an impulse for the coasting larva of Fig. 2 of 4.5×10^{-8} N s compared with 9.6×10^{-8} N s derived from the flow in the wake. For the adult fish, the impulse based on the coasting speed (1.4×10^{-4} N s) is larger than the estimate based on the wake (9.8×10^{-5} N s). Considering the poor spatial resolution of the flow fields, the estimates derived from the flow are in acceptable agreement with the impulse values derived from the coasting speed. McCutchen (1977) also quantified the flow around adult zebra danios performing a burst. His momentum balance is reversed compared with ours. However, when comparing our data with those of McCutchen (1977) for a fish performing a similar turn at a similar speed, McCutchen finds similar values for both the wake-based estimate (1.6×10^{-4} N s) and the coasting-speed-based value (0.8×10^{-4} N s).

Our estimates for the impulse of the wake are based on two assumptions about the vortex ring geometry. First, we assume circular vortex rings. Second, the cross-sectional area and the flow velocities in the two vortices comprising the cross section through the ring should be the same. The radius of the larval and adult vortex rings (0.8 and 8 mm, respectively) is roughly equivalent to the height of their tail fin (0.5 and 7 mm, respectively). We assume that the 'vertical' elements of the vortex ring are formed by the tail vortices as seen in our cross-sectional flow fields. The 'horizontal' elements are formed by the tip vortices of the tail. If we assume that the distance between the tip vortices is equivalent to the height of the tail, the fish would shed oval vortex rings, with the vertical diameter being half the horizontal diameter. Since our energy estimates are based on the horizontal dimensions, this might lead to an overestimation of the vortex ring momentum. The flow velocities in the second compared with the first vortex shed in the wake are identical in the larval vortices. The core flow velocity in the adult stop vortex at its moments of shedding is 25 % slower than that of the first shed vortex flow. However, these flow velocities soon equalize.

Energetic consequences of the flow regime

A burst-and-coast swimming style relies mainly on reactive

forces and unsteady effects for propulsion (Daniel and Webb, 1987). During the burst phase, the fish needs to generate momentum to accelerate to a terminal speed. During the coast phase, the fish exploits the fact that the drag of its straight body is lower than the drag of its undulating body. The higher the ratio of swimming to coasting drag, the more advantageous becomes a burst-and-coast swimming style. Weihs (1980) predicts that burst-and-coast swimming should become favourable for fish larvae at a body length above 5 mm. Considering the water temperature and body length of our zebra danio larvae, at their current average swimming speeds of $1\,L\,s^{-1}$, our larvae still have to spend 2–3 times as much energy swimming intermittently compared with swimming continuously. During fast bursts, the larvae reach Reynolds numbers above 20, at which coasting becomes feasible.

These predictions about the detrimental effects of viscosity on an intermittently swimming larva become obvious in the flow fields during the burst as well as the coast phase. During the burst phase, zebra danio larvae perform single tail flicks with little transverse movement of the more anterior body parts. This swimming style probably uses reactive forces for thrust generation: the flow velocities are highest where we would expect them if pressure effects were dominant, i.e. close to the points of maximum lateral excursion of the body. The flow fields do not resemble computational flow fields for undulatory propulsion at very low Reynolds numbers, where the highest flow velocities centre around the inflexion points of the body and thrust production is stress-based rather than pressure-based (Fauci, 1998). The oscillating movement of the tail accelerates the fluid rearwards and induces vortex shedding at the tail. These vortices combine to form a vortex ring containing the momentum that the fish added to the water in an attempt to gain equal forward momentum. However, the viscous length scale at these low Reynolds numbers is of the same size as the radius of the vortex ring and core. This means that the circulation of the vortex ring is expensive to maintain, and viscous diffusion quickly consumes the vortex ring. As a consequence, fish larvae shed large-core vortices that die off within less than 1 s (Fig. 2).

In adults, the viscous length scale is much smaller than the core of the vortex ring. Adult vortex rings have a relatively smaller core, and the ring dies off much more slowly. Hence, although both larvae and adult shed vortex rings to transfer momentum to the water and propel themselves, larvae are faced with much higher costs as a result of viscous effects.

During the coasting phase, larvae again pay a higher price because of viscous effects. At Reynolds numbers below 20, coasting is possible. But the ratio of swimming to coasting drag is much less beneficial than for adult fish. This high drag becomes tangible when the flow field around a coasting larva is examined. Elevated vorticity adjacent to the larva's body (Fig. 4) indicates the area over which the larva loses energy to the water. Flow velocities are elevated to the left and right of the larva, causing the total flow field to resemble the flow around a bluff body at low Reynolds number. A coasting adult produces a very different flow field. Flow velocities are elevated mainly in the wake behind the animal, the flow in the wake pointing towards the animal. Vorticity is considerably lower in the adult flow field and more concentrated in the wake rather than next to the body. The overall pattern is typical for a streamlined body in a flow at high Reynolds numbers (Prandtl and Tietjens, 1934; Aleyev, 1977). No large separation effects are visible around the body, and the fish develops a thin boundary layer beyond the spatial resolution of our flow field. The main features of the flow pattern are the source effect of the head and the decelerated flow in the wake.

The dominance of viscous over inertial effects seriously impairs the larva's performance in the coasting phase. The enormous viscous losses reduce the larva's coasting distance to half a body length. Adult fish can coast for several body lengths, but usually choose to initiate another burst before their terminal burst speed has halved.

During the fast burst, the zebra danio larva reached a swimming speed comparable with the escape speeds measured by Fuiman and Webb (1988). The flow pattern of the larval fast burst deviates from the adult flow pattern in the same way as the slow burst pattern. Although Fuiman and Webb (1988) showed that 95 % of the escape behaviour takes place in the inertial flow regime, the initiation of even a fast tail flick occurs at Reynolds numbers low enough for the viscous flow pattern with its vortical flows next to the larva's body to develop (Fig. 6). Adult fish, in contrast, only generate a vortex ring, shed at the end of the tail flick (Fig. 3).

Theoretical (Weihs, 1980) and kinematic (Hunter, 1972; Batty, 1984; Osse and Drost, 1989; Fuiman and Batty, 1997) evidence suggests that small fish larvae are exposed to considerable viscous forces. Hence, while in a low-Reynolds-number realm, fish larvae choose a continuous swimming style (Hunter, 1972; Vlymen, 1974; Batty, 1984, 1981). At the transition from a viscous to an inertial flow regime, zebra danios, like other fish larvae (Weihs, 1980), exhibit a continuum of swimming styles from continuous to burst-and-coast. The flow fields generated by zebra danio larvae confirm that fish larvae employing a burst-and-coast swimming style do so at considerable costs compared with adult fish. Larval fish gain much less from a burst-and-coast swimming style than adults, but this style might enable them to escape the viscous realm at lower body lengths by reaching higher swimming speeds than during continuous swimming.

List of symbols and abbreviations

a	mean ring radius of a large-core vortex ring
C	closed curve around a vortex
d	discriminant for complex eigenvalues
L	body length
$\mathbf{m}$	vortex velocity vector
R	ring radius of a small-core vortex ring
Re	Reynolds number
p	impulse of the vortex ring
t	time since the onset of a burst
T	tail-beat period

U_m	maximum swimming speed reached during a burst
U_t	swimming speed at the transition from the burst to the coasting phase
u	flow velocity component in X'
v	flow velocity component in Y'
v_0	terminal velocity
x,y	original image coordinates
X,Y	Cartesian coordinates of the swimming fish
X',Y'	Cartesian coordinates of the vortex ring
α	non-dimensionalised mean core radius of a vortex ring
β	angle of the jet through a vortex ring
ε	radius of the vortex core
Γ	circulation of a vortex ring
φ	momentum angle of the vortex ring
ν	kinematic viscosity of water
ρ_{water}	density of water
ω	vorticity
ω_{max}	maximum vorticity

E.J.S. wrote most of the data-processing software. The project was part of the PhD of U.K.M. under the supervision of J.J.V. We would like to thank the Department of Developmental Genetics, in particular E. Bijmolt, M. Drost and M. Ferwerda, for providing the adult zebra danios and for caring for the larval fish. The comments of L. A. Fuiman, T. J. Pedley and D. Weihs helped considerably to improve the manuscript.

References

Acheson, D. J. (1990). *Elementary Fluid Dynamics*. New York: Oxford University Press. 397pp.

Aleyev, Y. G. (1977). *Nekton*. The Hague: Dr W. Junk. 435pp.

Bailey, K. M. and Batty, R. S. (1984). Laboratory study of predation by *Aurelia aurita* on larvae of cod, flounder, plaice and herring: development and vulnerability to capture. *Mar. Biol.* **83**, 287–291.

Batchelor, G. K. (1967). *Fluid Dynamics*. Cambridge: Cambridge University Press. 615pp.

Batty, R. S. (1981). Locomotion in plaice larvae. In *Vertebrate Locomotion* (*Symposia of the Zoological Society of London*) (ed. M. H. Day), pp. 53–69. London: Academic Press.

Batty, R. S. (1984). Development of swimming movements and musculature of larval herring (*Clupea harengus*). *J. Exp. Biol.* **110**, 217–229.

Chen, C. J., Kim, Y. G. and Walter, J. A. (1993). Progress in quantitative flow visualisation and imaging process. In *Atlas of Visualisation* (The Visualization Society of Japan), pp. 279–296. Oxford: Pergamon Press.

Daniel, T. L. and Webb, P. W. (1987). Physical determinants of locomotion. In *Comparative Physiology: Life in Water and on Land, Fidia Research Series*, vol. 9 (ed. P. Dejours, L. Bolis, C. R. Taylor and E. R. Weibel), pp. 343–369. Padova: Livinia Press.

Darbrowski, K. R., Kok, L. Y. and Takashima, F. (1986). How efficiently do fish larvae and juveniles swim? *Comp. Biochem. Physiol.* **85**A, 657–661.

Fauci, L. J. (1998). A computational model of the fluid dynamics of undulatory and flagellar swimming. *Am. Zool.* **36**, 599–607.

Fuiman, L. A. (1983). Growth gradients in fish larvae. *J. Fish Biol.* **23**, 117–123.

Fuiman, L. A. (1986). Burst swimming performance of larval zebra danios and the effect of dial temperature fluctuations. *Trans. Am. Fish. Soc.* **115**, 143–148.

Fuiman, L. A. and Batty, R. S. (1997). What a drag it is getting cold: partitioning the physical and physiological effects of temperature on fish swimming. *J. Exp. Biol.* **200**, 1745–1755.

Fuiman, L. A. and Webb, P. W. (1988). Ontogeny of routine swimming activity and performance in zebra danios (Teleostei: Cyprinidae). *Anim. Behav.* **36**, 250–261.

Galloway, T. F., Kjørsvik, E. and Kryvi, H. (1999). Muscle growth and development in Atlantic cod larvae (*Gadus morhua* L.) related to different somatic growth rates. *J. Exp. Biol.* **202**, 2111–2120.

Gray, J. and Hancock, G. J. (1955). The propulsion of sea-urchin spermazoa. *J. Exp. Biol.* **32**, 802–814.

Hunter, J. R. (1972). Swimming and feeding behaviour of larval anchovy *Engraulis mordax*. *Fishery Bull.* **70**, 821–838.

Kaufmann, R. (1990). Respiratory cost of swimming in larval and juvenile cyprinids. *J. Exp. Biol.* **150**, 343–366.

Kumar, M., Arakeri, J. H. and Shankar, P. N. (1995). Translational velocity oscillations of piston generated vortex rings. *Phys. Fluids* **7**, 2751–2756.

Lamb, H. (1932). *Hydrodynamics*. 6th edition. Cambridge: Cambridge University Press. 738pp.

Lighthill, M. J. (1960). Note on swimming of slender fish. *J. Fluid Mech.* **9**, 305–317.

Lighthill, M. J. (1969). Hydromechanics of aquatic animal locomotion. *Annu. Rev. Fluid Mech.* **1**, 413–446.

McCutchen, C. W. (1977). Froude propulsive efficiency of a small fish, measured by wake visualisation. In *Scale Effects in Animal Locomotion* (ed. T. J. Pedley), pp. 339–363. London: Academic Press.

Müller, U. K. and Videler, J. J. (1996). Inertia as a 'safe harbour': do fish larvae increase length growth to escape viscous drag*? Rev. Fish Biol. Fish.* **6**, 353–360.

Norbury, J. (1973). A family of steady vortex rings. *J. Fluid Mech.* **57**, 417–431.

Osse, J. W. M. (1990). Form changes in fish larvae in relation to changing demands of function. *Neth. J. Zool.* **40**, 362–385.

Osse, J. W. M. and Drost, M. R. (1989). Hydrodynamics and mechanics of fish larvae. *Pol. Arch. Hydrobiol.* **36**, 455–465.

Prandtl, L. and Tietjens, O. G. (1934). *Applied Hydro- and Aerodynamics*. New York: Dover. 311pp.

Spedding, G. R. (1986). The wake of a jackdaw (*Corvus monedula*) in slow flight. *J. Exp. Biol.* **125**, 287–307.

Spedding, G. R. (1987). The wake of a kestrel (*Falco tinnunculus*) in flapping flight. *J. Exp. Biol.* **127**, 59–78.

Spedding, G. R., Rayner, J. M. V. and Pennycuick, C. J. (1984). Momentum and energy in the wake of a pigeon (*Columbia livia*) in slow flight. *J. Exp. Biol.* **111**, 81–102.

Stamhuis, E. J. and Videler, J. J. (1995). Quantitative flow analysis around aquatic animals using laser sheet particle image velocimetry. *J. Exp. Biol.* **198**, 283–294.

van Dyke, M. (1982). *An Album of Fluid Motion*. Stanford: The Parabolic Press. 176pp.

Vlymen, W. J. (1974). Swimming energetics of the larval anchovy, *Engraulis mordax*. *Fishery Bull.* **72**, 885–899.

Vollmers, H., Kreplin, H.-P. and Meier, H. U. (1983). Separation

and vortical-type flow around a prolate sphereoid – evaluation of relevant parameters. *NATO AGARD Conference Proceedings* **342**, 14/1–14/14.

Wardle, C. S., Videler, J. J. and Altringham, J. D. (1995). Tuning in to fish swimming waves: body form, swimming mode and muscle function. *J. Exp. Biol.* **198**, 1629–1636.

Webb, P. W. and Weihs, D. (1986). Functional locomotor morphology of early life history stages of fishes. *Trans. Am. Fish. Soc.* **115**, 115–127.

Weihs, D. (1974). Energetic advantages of burst swimming of fish. *J. Theor. Biol.* **48**, 215–229.

Weihs, D. (1980). Energetic significance of changes in swimming modes during growth of larval anchovy, *Engraulis mordax*. *Fishery Bull.* **77**, 597–604.